



1 **FRONT MATTER**

2 **Title**

3 Mid-Holocene Antarctic sea-ice increase driven by marine ice sheet retreat

4 **Authors**

5 Kate E. Ashley^{1*}, James A. Bendle¹, Robert McKay², Johan Etourneau³, Francis J. Jimenez-Espejo^{3,4},
6 Alan Condron⁵, Anna Albot², Xavier Crosta⁶, Christina Riesselman^{7,8}, Osamu Seki⁹, Guillaume Massé¹⁰,
7 Nicholas R. Golledge^{2,11}, Edward Gasson¹², Daniel P. Lowry², Nicholas E. Barrand¹, Katelyn Johnson²,
8 Nancy Bertler², Carlota Escutia³ and Robert Dunbar¹³.

9 **Affiliations**

10 ¹School of Geography, Earth and Environmental Sciences, University of Birmingham, Edgbaston,
11 Birmingham, B15 2TT, UK

12 ²Antarctic Research Centre, Victoria University of Wellington, Wellington 6140, New Zealand

13 ³Instituto Andaluz de Ciencias de la Tierra (CSIC), Avenida de las Palmeras 4, 18100 Armilla, Granada,
14 Spain

15 ⁴Department of Biogeochemistry, Japan Agency for Marine-Earth Science and Technology
16 (JAMSTEC), Yokosuka 237-0061, Japan

17 ⁵Department of Geology and Geophysics, Woods Hole Oceanographic Institution, Woods Hole, MA
18 02543, USA

19 ⁶UMR-CNRS 5805 EPOC, Université de Bordeaux, 33615 Pessac, France

20 ⁷Department of Geology, University of Otago, Dunedin 9016, New Zealand

21 ⁸Department of Marine Science, University of Otago, Dunedin 9016, New Zealand

22 ⁹Institute of Low Temperature Science, Hokkaido University, Sapporo, Hokkaido, Japan

23 ¹⁰TAKUVIK, UMI 3376 UL/CNRS, Université Laval, 1045 avenue de la Médecine, Quebec City,
24 Quebec, Canada G1V 0A6

25 ¹¹GNS Science, Avalon, Lower Hutt 5011, New Zealand

26 ¹²Department of Geography, University of Sheffield, Winter Street, Sheffield, S10 2TN, UK

27 ¹³Department of Environmental Earth Systems Science, Stanford University, Stanford, CA 94305-2115

28

29 ***Corresponding Author:** email: ken155@student.bham.ac.uk



30

31 1. ABSTRACT

32 Over recent decades Antarctic sea-ice extent has increased, alongside widespread ice shelf thinning and
33 freshening of waters along the Antarctic margin. In contrast, Earth system models generally simulate a
34 decrease in sea ice. Circulation of water masses beneath large cavity ice shelves is not included in current
35 models and may be a driver of this phenomena. We examine a Holocene sediment core off East Antarctica
36 that records the Neoglacial transition, the last major baseline shift of Antarctic sea-ice, and part of a late-
37 Holocene global cooling trend. We provide a multi-proxy record of Holocene glacial meltwater input,
38 sediment transport and sea-ice variability. Our record, supported by high-resolution ocean modelling,
39 shows that a rapid Antarctic sea-ice increase occurred against a backdrop of increasing glacial meltwater
40 input and gradual climate warming. We suggest that mid-Holocene ice shelf cavity expansion led to
41 supercooling of surface waters and sea-ice growth which slowed basal ice shelf melting. Incorporating
42 this feedback mechanism into global climate models will be important for future projections of Antarctic
43 changes.

44

45 2. INTRODUCTION

46 Ice shelves and sea ice are intrinsically linked and represent fundamental components of the global
47 climate system, impacting ice-sheet dynamics, large-scale ocean circulation, and the Southern Ocean
48 biosphere. Antarctic ice-shelves with large sub-shelf cavities (e.g. Ross, Filchner-Ronne) play a key role
49 in regional sea-ice variations, by cooling and freshening surface ocean waters for hundreds of kilometres
50 beyond the ice shelf edge (Hellmer, 2004; Hughes *et al.*, 2014). Antarctic sea ice has expanded over the
51 past few decades, particularly in the western Ross Sea region (Turner *et al.*, 2016), alongside widespread
52 thinning of ice shelves (Paolo *et al.*, 2015) and freshening along the Antarctic margin (Jacobs *et al.*,
53 2002; Aoki *et al.*, 2013). The drivers and feedbacks involved in these decadal trends are still poorly
54 understood, hampered by the sparse and short-term nature of meteorological, oceanographic and
55 glaciological observations (Jones *et al.*, 2016), and thus establishing the long-term trajectory for
56 Antarctic sea ice on the background of accelerated ice sheet loss remains a challenge. Marine sediment
57 cores provide a longer-term perspective and highlight a major baseline shift in coastal sea ice ~4.5 ka
58 ago (Steig *et al.*, 1998; Crosta *et al.*, 2008; Denis *et al.*, 2010) which characterizes the mid-Holocene
59 ‘Neoglacial’ transition in the Antarctic. A mechanistic driver for this climate shift currently remains



60 unresolved, but we propose that two interrelated aspects of the last deglaciation are significantly
61 underrepresented in current models of this transition: (i) the retreat of grounded ice sheets from the
62 continental shelves of Antarctica, and (ii) the subsequent development of large ice shelf cavities during
63 the Holocene. Both factors would significantly alter water mass formation on Antarctica's continental
64 shelves, which today are major source regions of Antarctic Bottom Water (AABW) and Antarctic
65 Surface Water (AASW). These interrelated processes are underrepresented in coupled ocean-atmosphere
66 models which currently do not simulate the timing, magnitude and rapid onset of the Neoglacial
67 (Supplementary Materials).

68

69 Integrated Ocean Drilling Program (IODP) Expedition 318 cored a 171 m thick deposit of laminated
70 diatomaceous ooze at Site U1357 offshore Adélie Land (Fig. 1), deposited over the past 11,400 years.
71 Here, we present a new Holocene record of glacial meltwater, sedimentary input and local sea ice
72 concentrations from Site U1357 using compound-specific hydrogen isotopes of fatty acid biomarkers
73 ($\delta^2\text{H}_{\text{FA}}$), terrigenous grain size, biogenic silica accumulation, highly-branched isoprenoid alkenes (HBIs)
74 and Ba/Ti ratios (Fig. 2 and S4).

75

76 We interpret $\delta^2\text{H}_{\text{FA}}$ (Fig. 2) fluctuations in Adélie Drift sediments as a record of meltwater input from
77 isotopically-depleted glacial ice (Supplementary Materials). Antarctic glacial ice is highly depleted in ^2H
78 compared to ocean water, thus creating highly contrasting end-member values for the two major H
79 source pools. Grain size (sand and mud percentage and sorting), natural gamma radiation (NGR) and
80 terrigenous and biosiliceous mass accumulation rates (MARs) reflect changing sediment delivery either
81 driven via local glacial meltwater discharge or advection of suspended sediment by oceanic currents.
82 The diene/triene HBI ratio is used as a proxy for coastal sea ice presence (Massé *et al.*, 2011). Ba/Ti
83 enrichment is considered to reflect enhanced primary productivity. These records allow a unique
84 opportunity to reconstruct the magnitude of the coupled response of the ocean and ice sheet during the
85 Neoglacial transition. Details on all proxies and associated uncertainties can be found in Section 4.2 and
86 in the Supplementary Materials.

87

88

89 3. MATERIALS AND METHODS

90



91 3.1 Organic geochemical analyses

92 Lipid extraction of sediment samples was performed at the Royal Netherlands Institute for Sea Research
93 (NIOZ). Freeze-dried and homogenized samples were extracted by Dionex™ accelerated solvent
94 extraction (DIONEX ASE 200) using a mixture of dichloromethane (DCM)/methanol (MeOH) (9:1,
95 v/v) at a temperature of 100°C and a pressure of 7.6×10^6 Pa (Kim *et al.*, 2010).

96

97 Two-thirds of the total lipid extract were sent to the University of Glasgow, UK and separated over an
98 aminopropyl silica gel column where the total neutral fraction was eluted with 4ml of DCM/ isopropanol
99 (1:1 v/v), and the total acid fractions were eluted into an 8ml vial with 4% acetic acid in ethyl-ether
100 solution (Huang *et al.*, 1999). Derivatisation to Fatty Acid Methyl Esters was achieved by adding 200 µl
101 of MeOH containing 14% v/v Boron trifluoride to the 8ml vial containing the TAF. The vial was seal
102 and placed in the drying cabinet at 70°C for one hour. The MeOH was dried under N₂ and the FAMES
103 were recovered and cleaned up by eluting through a pre-cleaned 3cm silica gel column (60 Å; 35-70)
104 with 4ml of hexane and 4ml of DCM (containing the FAMES). The recovered FAMES fraction was
105 split 50:50 for compound specific carbon and hydrogen analysis, respectively. $\delta^2\text{H}$ values indicate
106 depletion against the international standards: Vienna Pee Dee Belemnite (V-PDB) is the standard for
107 $\delta^{13}\text{C}$ and Vienna Standard Mean Ocean Water (V-SMOW) for $\delta^2\text{H}$.

108

109 Compound specific hydrogen isotope analyses of FAMES was performed at the Institute of Low
110 Temperature Science, Hokkaido University. $\delta^2\text{H}$ values were obtained using a CS-IRMS system with a
111 HP 6890 gas chromatograph and a ThermoQuest Finnigan MAT Delta Plus XL mass spectrometer.
112 Separation of the FAMES was achieved with a HP-5 MS fused silica capillary column (30 m x 0.32 mm
113 i.d., film thickness of 0.25 µm) with a cooled on-column injector. An *n*-alkane and a reference gas
114 whose isotopic values were known was co-injected with the samples as an internal isotopic standard for
115 $\delta^2\text{H}$. A laboratory standard (Mix F8 of FAMES from Indiana University) containing C₁₀–C₃₀ FAMES
116 was analyzed daily to check the accuracy and the drift of the instrument and to normalize the data to the
117 SMOW/SLAP isotopic scale. The H³⁺ factor was measured every three days.

118

119 3.2 Inorganic geochemical analysis and electronic microscopy

120 Major element concentrations were obtained using X-Ray Fluorescence Scanner on 412 analyses
121 measured directly over undisturbed sediment sections. The bulk major element composition included in



122 this study was measured between sections U1357B-1H-2 to U1357-19H-5 continuously each 50 cm. We
123 used an Avaatech X-ray fluorescence (XRF-Scanner) core scanner at the IODP-Core Repository/Texas
124 A&M University laboratories (USA) during December 2010. Non-destructive XRF core-scanning
125 measurements were performed over 1 cm² area with slit size of 10 mm, a current of 0.8 mA and
126 sampling time of 45 seconds at 10 kV in order to measure the relative content of titanium (Ti) and
127 barium (Ba).

128

129 Field emission scanning electron microscopy (FESEM) images and corresponding spectrum were
130 obtained with an AURIGA FIB-FESEM Carl Zeiss SMT at Centro de Instrumentación Científica,
131 Granada University, Spain

132

133 **3.3 Grain size analyses**

134 A total of 341 samples were prepared for grain size analysis. Samples were treated for removal of
135 biogenic opal with a 1M sodium hydroxide NaOH solution and incubated in a water bath at 80°C for 24
136 hours. This procedure was repeated twice due to an incomplete dissolution of diatoms observed in smear
137 slides. The samples were then treated with H₂O₂ to remove organic material at 80°C for 24 hours.
138 Samples were measured using a Beckman Coulter LS 13 320 Laser Diffraction Particle Size Analyser
139 (LPSA). The LPSA has a relatively narrow range of optimum obscuration which is determined by the
140 sample surface area, in turn determined by sample concentration and sample distribution. Prior to grain
141 size analysis, ~30 mL of 0.5 g/L Calgon (sodium hexametaphosphate) was added to the samples, and
142 sonicated and stirred in order to disperse the grains and prevent clumping. The range in sample mass for
143 most of the post-treatment samples varied from ~0.035-0.8 grams. Random biases propagating through
144 this process cannot be ruled out, especially when taking account of susceptibility of grains <10 µm to
145 clump (McCave *et al.*, 1995) and random cohesion of grains due to any remaining organic content. The
146 aqueous liquid module in the LPSA also does not accurately record the <2 µm clay that may
147 compromise a significant part of the size spectrum in glacial environments (McCave *et al.*, 1995;
148 McCave and Hall, 2006). Given these considerations, subsamples were taken from a total of 84 samples
149 to test reproducibility of the data relating to sub-sampling biases, with a least squares regression
150 showing a high reproducibility with an r² value of 0.744. An additional 12 samples were sub-sampled
151 before the chemical treatment in order to test the reproducibility of the treatment methodology, with a
152 least squares regression showing a high reproducibility with an r² value of 0.752.



153

154 **3.4 HBIs**

155 Highly branched isoprenoids (HBI) alkenes were extracted at Laboratoire d'Océanographie et du
156 Climat: Experimentations et Approches Numériques (LOCEAN), separately from the fatty acids, using a
157 mixture of 9mL CH₂Cl₂/MeOH (2:1, v:v) to which internal standards were added and applying several
158 sonication and centrifugation steps in order to extract properly the selected compounds (Étourneau *et al.*,
159 2013). After drying with N₂ at 35°C, the total lipid extract was fractionated over a silica column into an
160 apolar and a polar fraction using 3 mL hexane and 6 mL CH₂Cl₂/MeOH (1:1, v:v), respectively. HBIs
161 were obtained from the apolar fraction by the fractionation over a silica column using hexane as eluent
162 following the procedures reported by Belt *et al.* (2007; Massé *et al.*, 2011). After removing the solvent
163 with N₂ at 35°C, elemental sulfur was removed using the TBA (Tetrabutylammonium) sulfite method
164 (Jensen *et al.*, 1977; Riis and Babel, 1999). The obtained hydrocarbon fraction was analyzed within an
165 Agilent 7890A gas chromatograph (GC) fitted with 30 m fused silica Agilent J&C GC column (0.25 mm
166 i.d., 0.25 µm film thickness), coupled to an Agilent 5975C Series mass selective detector (MSD).
167 Spectra were collected using the Agilent MS-Chemstation software. Individual HBIs were identified on
168 the basis of comparison between their GC retention times and mass spectra with those of previously
169 authenticated HBIs (Johns *et al.*, 1999) using the Mass Hunter software. Values are expressed as
170 concentration relative to the internal standard.

171

172 **3.5 Biogenic silica**

173 Biogenic silica concentrations (wt% BSi) were measured on 349 discrete samples using a molybdate
174 blue spectrophotometric method modified from (Strickland and Parsons, 1970; DeMaster, 1981).
175 Analytical runs included replicates from the previous sample group and from within the run, and each
176 run was controlled by 10 standards and a blank with dissolved silica concentrations ranging from 0 µM
177 to 1200 µM. For each analysis, ~7 mg of dry, homogenized sediment was leached in 0.1M NaOH at
178 85°C, and sequential aliquots were collected after 2, 3, and 4 hours. Following addition of reagents,
179 absorbance of the 812 nm wavelength was measured using a Shimadzu UV-1800 spectrophotometer.
180 Dissolved silica concentration of each unknown was calculated using the standard curve, and data from
181 the three sampling hours were regressed following the method of DeMaster (1981) to calculate wt%
182 BSi. In our U1357B samples, wt% BSi ranges from maximum of ~60% in early and mid-Holocene light



183 laminae to a minimum of 31% in late Holocene dark laminae. The average standard deviation of
184 replicate measurements is 0.5%.

185

186 **3.6 Model simulations**

187 All numerical calculations were performed using the Massachusetts Institute of Technology general
188 circulation model (MITgcm) (Marshall *et al.*, 1997); a three-dimensional, ocean sea-ice, hydrostatic,
189 primitive equation model. The experiments presented here were integrated on a global domain projected
190 onto a cube-sphere grid to permit a relatively even grid spacing and to avoid polar singularities (Adcroft
191 *et al.*, 2004; Condrón and Winsor, 2012). The ocean grid had a mean, eddy-permitting, horizontal grid
192 spacing of $1/6^\circ$ (18-km) with 50 vertical levels ranging in thickness from 10m near the surface to
193 approximately 450m at the maximum model depth. The ocean model is coupled to a sea-ice model in
194 which ice motion is driven by forces generated by the wind, ocean, Coriolis force, and surface elevation
195 of the ocean, while internal ice stresses are calculated using a viscous-plastic (VP) rheology, as
196 described in Zhang and Hibler (1997). In all experiments, the numerical model is configured to simulate
197 present-day (modern) conditions: Atmospheric forcings (wind, radiation, rain, humidity etc.) are
198 prescribed using 6-hourly climatological (1979-2000) data from the ERA-40 reanalysis product
199 produced by the European Centre for Medium-range Weather Forecasts and background rates of runoff
200 from the ice sheet to the ocean are based on the numerical ice sheet model of Pollard and Deconto
201 (2016) integrated over the same period (1979-2000). To study the pathway of meltwater in the ocean,
202 additional fresh (i.e. 0 psu) water was released into the surface layer of the ocean model at the grid
203 points closest to the front of the Ross Ice Shelf. Five different discharge experiments were performed by
204 releasing meltwater into this region at rates of 0.01 Sv ($\text{Sv} = 10^6 \text{ m}^3/\text{s}$), 0.05 Sv, 0.1 Sv, 0.5 Sv, and 1 Sv
205 for the entire duration of each experiment (~3.5 years).

206

207 **4. ENVIRONMENTAL SETTING AND INTERPRETATION OF PROXY DATA**

208 We utilize a 180 m thick sediment core that was recovered from the Wilkes Land Margin continental
209 shelf in the Adélie Basin (IODP Site U1357). This core targeted an expanded sediment drift (Adélie
210 Drift) and provides a high-resolution Holocene record of climate variability. Below we provide pertinent
211 details on this unique site and on our application of compound specific $\delta^2\text{H}$ measurements on algal
212 biomarkers as a novel meltwater proxy. Further details on proxy interpretation (Ba/Ti, grain size, HBIs)
213 are given in the Supplementary Materials.



214

215 **4.1 The Adélie Drift**

216 Site U1357 is located in the Dumont d'Urville Trough of the Adélie Basin, ca. 35 km offshore from
217 Adélie Land (66°24.7990'S, 140°25.5705'E; Fig 1). This is a >1000 m deep, glacially scoured
218 depression on the East Antarctic continental shelf, bounded to the east by the Adélie Bank. Further east
219 lays the Adélie Depression and the Mertz Bank, the latter located north of the Mertz Glacier floating ice
220 tongue. The Adélie Land region is dissected by several glaciers which could potentially contribute
221 terrigenous sediment into the coastal zone with the core site located 40 km to the north of the Astrolabe
222 Glacier, and ca. 75 and 300 km northwest of the Zélée and Mertz glaciers, respectively.

223

224 The site itself is located within the Dumont d'Urville polynya (DDUP), which has a summer (winter)
225 extent of 13,020 km² (920 km²), but is also directly downwind and downcurrent of the much larger and
226 highly productive Mertz Glacier polynya (MGP) to the east, with a summer (winter) extent of 26,600
227 km² (591 km²) (Arrigo and van Dijken, 2003). The MGP forms as a result of reduced sea-ice westward
228 advection due to the presence of the Mertz Glacier Tongue (Massom *et al.*, 2001) and strong katabatic
229 winds which blow off the Antarctic ice sheet with temperatures below -30°C (Bindoff *et al.*, 2000).
230 Katabatic winds freeze the surface waters and blow newly formed ice away from the coast, making the
231 polynya an efficient sea-ice 'factory', with higher rates of sea-ice formation in comparison to non-
232 polynya ocean areas which undergo seasonal sea ice formation (Kusahara *et al.*, 2010). The MGP
233 produces 1.3% of the total Southern Ocean sea ice volume despite occupying less than 0.1% of total
234 Antarctic sea ice extent (Marsland *et al.*, 2004).

235

236 As a result of the upwelling polynya environments, the area along the Adélie Coast is characterized by
237 extremely high primary productivity, with the water column known to host significant amounts of
238 phytoplankton, dominated by diatoms (Beans *et al.*, 2008). The Mertz Glacier zone is generally
239 characterized by stratified waters in the summer, due to seasonal ice melt, with these conditions
240 corresponding to the highest phytoplankton biomass. The lack of ice cover means polynyas are the first
241 polar marine systems exposed to spring solar radiation, making them regions of enhanced biological
242 productivity compared to adjacent waters. A considerable amount of resultant sedimentation is focused
243 via the westward flowing currents from both of these polynyas within the deep, protected Adélie Basin,



244 resulting in a remarkably high sedimentation rate of ca. 1.5-2 cm year⁻¹ at Site U1357 (Escutia *et al.*,
245 2011).

246

247 Although biogenic and terrigenous sediment is interpreted to be sourced locally in the Adélie Land
248 region, the mass accumulation rate of these sediments in this drift is associated with the intensity of
249 westward flowing currents (S2.2). Critically, these westward currents also act to transport water masses
250 from further afield, and Site U1357 is directly oceanographically downstream of the Ross Sea, meaning
251 the continental shelf in this region receives significant Antarctic Surface Water (ASSW) transported by
252 the Polar Easterlies and the Antarctic Slope Current (ASC) from the Ross Sea embayment (Fig 3). Thus,
253 changes in the surface waters of the Ross Sea influence Site U1357. Whitworth *et al.* (1998) confirm the
254 continuity of the westward flowing ASC between the Ross Sea and the Wilkes Land margin. This flow
255 is largely associated with the Antarctic Slope Front, which reflects the strong density contrast between
256 AASW and Circumpolar Deep Water (CDW). McCartney and Donohue (2007) estimate that the
257 transport in the westward ASC, which links the Ross Sea to the Wilkes Land margin, reaches 76 Sv (106
258 m³ s⁻¹). This contributes to a cyclonic gyre, which together with the ASC dominate the circulation at Site
259 U1357. The gyre transports around 35 Sv, and comes mainly from the Ross Sea region, with a lesser
260 contribution from a westward flow associated with the Antarctic Circumpolar Current.

261 While several small glaciers within Adélie Land may contribute meltwater to the site, the region is also
262 likely to be influenced significantly by changes in Ross Sea waters. Freshwater release simulations from
263 the Ross Ice Shelf (RIS) confirm this oceanographic continuity between the Ross Sea and the Wilkes
264 region (Fig 3). Five simulations with fluxes from 0.01 to 1 Sv released from the edge of the RIS all
265 indicate that meltwater is almost completely entrained within the westward coastal surface current and
266 reaches Site U1357 within 4 months to 1 year (Fig 4). These fluxes cover a wide range of meltwater
267 inputs and show a strong linear relationship with salinity at the core site (Fig. 4). This suggests that the
268 magnitude of the signal recorded at Site U1357 is directly related to the magnitude of meltwater.

269 Local processes do also play a critical role in this region. For example, episodic calving events of the
270 Mertz Glacier tongue release fast ice over the drill site and create strong surface water stratification,
271 cutting off local AABW production (Campagne *et al.*, 2015). Although appearing to be only a local
272 process, there is still a regional (Ross Sea) influence, as this fast ice that builds up behind the Mertz
273 Glacier is formed by the freezing of fresher AASW transported from the Ross Sea (Fig 3). Thus,



274 conditions in the Ross Sea, such as the melting of isotopically depleted glacial ice, would influence both
275 the isotopic composition and amount of this sea ice.

276

277 **4.2 Site specific interpretation of $\delta^2\text{H}_{\text{FA}}$ as a glacial meltwater proxy**

278

279 **4.2.1. Source of fatty acids**

280 To best interpret the hydrogen isotope signal recorded by the C_{18} FA, it is important to determine the
281 most likely source these compounds are derived from, and thus the habitat in which they are produced.
282 The C_{18} FA, however, is known to be produced by a wide range of organisms and so we cannot preclude
283 the possibility of multiple sources, especially in a highly diverse and productive region such as the
284 surface waters of offshore Adélie Land. However, we can attempt to determine the most dominant
285 producer(s), which will help us understand the main signal being recorded by the isotopes.

286

287 An analysis of the FAs within eight classes of microalgae by Dalsgaard *et al.* (2003) (compiling results
288 from multiple studies) showed *Cryptophyceae*, *Chlorophyceae*, *Prasinophyceae* and *Prymnesiophyceae*
289 to be the most dominant producers of total C_{18} FAs. The *Bacillariophyceae* class, on the other hand,
290 which includes the diatoms, were found to produce only minor amounts of C_{18} FA, instead synthesizing
291 abundant $\text{C}_{16:1}$ FAs. Thus, despite the water column offshore Adélie Land being dominated by diatoms,
292 these are unlikely to be a major source of the C_{18} FA within U1357B (Beans *et al.*, 2008; Riaux-Gobin
293 *et al.*, 2011).

294

295 Of the four microalgae classes dominating C_{18} production (Dalsgaard *et al.*, 2003), species from the
296 Chlorophyceae and Prymnesiophyceae classes have been observed within surface waters offshore
297 Adélie Land after spring sea-ice break-up (Riaux-Gobin *et al.*, 2011). Here, *Phaeocystis antarctica* of
298 the Prymnesiophytes was found to dominate the surface water phytoplankton community (representing
299 16% of the phytoplankton assemblage), whereas Cryptophyceae spp. were found in only minor
300 abundances (Riaux-Gobin *et al.*, 2011). In the Antarctic, *Phaeocystis* is thought to be the most dominant
301 producer of C_{18} FAs (Dalsgaard *et al.*, 2003), and thus is likely to be a key producer of the C_{18} FA in
302 U1357B samples.

303



304 To investigate this further, we measured compound-specific carbon isotopes of the C₁₈ FAs in U1357B
305 samples, which gives an average δ¹³C value of -29.8 ± 1.0 ‰ (n=85). Budge *et al.* (2008) measured a
306 similar δ¹³C value of -30.7 ± 0.8‰ from C₁₆ FAs derived from Arctic pelagic phytoplankton, while sea
307 ice algae and higher trophic level organisms all had much higher δ¹³C values (sea ice algae having
308 values of -24.0 ± 2.4‰). Assuming similar values apply for the C₁₈ FA and for organisms within the
309 water column at our site, this suggests that our C₁₈ FA is predominantly derived from pelagic
310 phytoplankton.

311

312 Furthermore, δ¹³C measurements of suspended particulate organic matter (SPOM) near Prydz Bay, East
313 Antarctica by Kopczynska *et al.* (1995) showed that sites with high δ¹³C SPOM values (-20.1 to -
314 22.4‰) were characterized by diatoms and large heterotrophic dinoflagellates, whereas the lowest δ¹³C
315 SPOM values (-29.7 to -31.85‰) were associated with *Phaeocystis*, naked flagellates and autotrophic
316 dinoflagellates. Wong and Sackett (1978) measured the carbon isotope fractionation of seventeen
317 species of marine phytoplankton and showed that Haptophyceae (of which *Phaeocystis* belongs) had the
318 largest fractionation of -35.5‰.

319

320 Therefore, based on the known producers of C₁₈ FAs, observed phytoplankton assemblages within
321 modern surface waters offshore Adélie Land, and the δ¹³C value of C₁₈ FAs in U1357B samples, as
322 discussed above, we argue that the C₁₈ FA here is predominantly produced by *Phaeocystis* (most likely
323 *P. antarctica*), but with potential minor inputs from other algal species such as Cryptophytes or diatoms.

324

325 *Phaeocystis antarctica* is a major phytoplankton species within the Antarctic, dominating spring
326 phytoplankton blooms, particularly in the Ross Sea (DiTullio *et al.*, 2000; Schoemann *et al.*, 2005). It is
327 known to exist both within sea ice and in open water (Tang *et al.*, 2008) and has been observed in
328 surface waters in great abundance following spring sea-ice break-up, at both coastal and offshore sites in
329 Adélie Land (Riaux-Gobin *et al.*, 2011).

330

331 Although a large proportion of organic matter produced in the surface water is recycled in the upper
332 water column, the small fraction which is deposited in the sediment reaches the sea floor through large
333 particles sinking from above as “marine snow”. This export production includes large algal cells, fecal
334 pellets, zooplankton carcasses and molts, and amorphous aggregates (Mayer, 1993). In the Ross Sea,



335 aggregates of *P. antarctica*, have been observed to sink at speeds of more than 200 m day⁻¹, meaning
336 they could reach deep water very quickly (Asper and Smith, 1999). In this way, a proportion of the lipid
337 content of *P. antarctica* and other algae is transported and sequestered in the sediments.

338

339 Initial diagenesis is characterized by the preferential degradation of more labile organic compounds e.g.
340 sugars, proteins, amino acids. Proportionally, lipids are relatively recalcitrant compared to other
341 biological components and thus are more likely to be preserved as molecular biomarkers on geological
342 timescales, even where the rest of the organism may be completely degraded. The final proportion of
343 lipids that are preserved within sediments are affected by factors including the export production, O₂
344 content, residence time in the water column and at the sediment/water interface before deposition,
345 molecular reactivity, formation of macromolecular complexes, adsorption to mineral surfaces and
346 bioturbation (Meyers and Ishiwatari, 1993; Killips and Killips, 2004). Within lacustrine sediments, a
347 significant shift in FA distribution has been shown to occur younger than 100 years due to early
348 diagenesis, after which the FA distribution remains relatively unaffected by diagenesis (Matsuda, 1978),
349 thus major changes are assumed to reflect primary environmental signals on longer timescales such as in
350 our Holocene record. Due to the hyperproductivity of the surface waters offshore Adélie land, we
351 assume the dominant inputs of the C₁₈ FA are from algal sources in overlying waters and upcurrent
352 regions. Allochthonous inputs e.g. long-range aeolian transport of plant material are assumed to be
353 minimal.

354

355 **4.2.2. Interpretation of hydrogen isotopes**

356 Compound-specific H isotopes of algal biomarkers are a well-used climate proxy in sediments
357 throughout the Cenozoic (e.g. Pagani *et al.*, 2006; Feakins *et al.*, 2012). Although diagenetic alteration,
358 including H-exchange, is possible within sedimentary archives, this has shown to be minimal in
359 sediments younger than 20 Ma (Sessions *et al.*, 2004). Furthermore, if H-exchange had occurred, we
360 would expect $\delta^2\text{H}$ values between different FA chain lengths and closely spaced samples to be driven
361 towards homogeneity, yet large variability remains, suggesting this is not the case. Thus, we are
362 confident that our measured H isotopes are indicating a primary signal throughout the Holocene.

363



364 The $\delta^2\text{H}$ value preserved in biomarkers is known to be correlated, but offset, with the $\delta^2\text{H}$ of the water
365 from which the hydrogen was derived. Measured $\delta^2\text{H}$ can therefore be described as a function of either
366 the $\delta^2\text{H}$ of the water source, or the fractionation occurring between source water and the lipid ($\epsilon_{l/w}$) (i.e.
367 vital effects), in which various environmental factors play a part (Sachse *et al.*, 2012).

368

369 The main environmental factors controlling $\epsilon_{l/w}$ are salinity and temperature, with which $\delta^2\text{H}$ increases
370 by 1-4‰ per increase in practical salinity unit (psu) (Schouten *et al.*, 2006; Sachse *et al.*, 2012) and
371 decreases by 2-4‰ per degree C increase (Zhang *et al.*, 2009), respectively. The $\delta^2\text{H}_{\text{FA}}$ record from Site
372 U1357 displays an absolute range of ca. 123‰, and millennial to centennial scale variability with an
373 amplitude of ca. 50‰, throughout the core. This would imply extremely large and pervasive variations
374 in temperature (up to ca. 60°C) and salinity (up to 123 psu) if fractionation driven by either of these
375 factors were the main control. One study has shown the salinity of present day Adélie shelf waters to
376 vary between 34 and 34.8 psu (Bindoff *et al.*, 2000), while tetraether-lipid based subsurface (50-200 m)
377 temperature estimates from nearby Site MD03-2601 (about 50 km west of Site U1357) range from -0.17
378 to 5.35°C over the Holocene (Kim *et al.*, 2010). Therefore, fractionation changes driven by temperature
379 or salinity cannot be invoked as a major control on $\delta^2\text{H}_{\text{FA}}$ in the Holocene.

380

381 Thus, the most parsimonious explanation relates to changes in $\delta^2\text{H}_{\text{FA}}$ of the water source (Sachse *et al.*,
382 2012). In the Adélie Basin, the most apparent controls on this are advection, upwelling or inputs of
383 isotopically depleted glacial meltwater. The $\delta^2\text{H}_{\text{FA}}$ value within Antarctic glaciers is highly depleted
384 relative to sea water due to the Rayleigh distillation process, leading to highly negative isotope values
385 for precipitation over the continent.

386

387 The glacial meltwater originating from the Ross Ice Shelf is likely to combine ice precipitated
388 throughout the Holocene and glacial period, and from both the East and West Antarctic Ice Sheets.
389 However, as noted by Shackleton and Kennett (1975) in their first oxygen isotope record of the
390 Cenozoic (see their Fig. 6), most of the ice that melts around the margin has been coastally precipitated
391 (due to higher accumulation rates). Since ice precipitated further inland has a greater residence time
392 (Shackleton and Kennett, 1975) and significantly lower accumulation rates it will contribute
393 significantly less to this signal. Thus, the ice that contributed to a marine-based ice sheet collapse along
394 this margin is best represented by average values of coastal ice dome records at a similar latitude to that



395 which melted since the LGM (such as TALDICE and Siple Dome) than more southerly locations.
396 Glacial to Holocene $\delta^2\text{H}_{\text{FA}}$ values from TALDICE, located on the western edge of the Ross Sea in the
397 East Antarctic, for example, vary between -276.2 and -330.3‰ (Steig *et al.*, 1998) (converted from $\delta^{18}\text{O}$
398 values following the global meteoric water line (GMWL): $\delta^2\text{H}_{\text{FA}} = 8.13 (\delta^{18}\text{O}) + 10.8$), while values
399 from Siple Dome on the eastern edge of the Ross Sea in the West Antarctic, vary from ca. -200 to -
400 293‰ (Brook *et al.*, 2005). Taking the average of these values as a rough estimate for the meltwater
401 gives a $\delta^2\text{H}$ value of ca. -275‰. We note our calculations are based on averages of set time periods,
402 which we expect would integrate ice of various ages - rather than extreme values which could relate to
403 specific melt events of ice or biases to certain ages/regions. This seems reasonable - the isotopic signal
404 of coastal surface waters masses advected from the RIS to the Adélie land (as illustrated in Fig. 3 and 4)
405 must integrate a range of source areas across the RIS and from the coast around to Adélie Land.

406

407 In comparison to the highly negative glacial ice isotope composition, sea surface water $\delta^{18}\text{O}$
408 measurements taken near the Mertz Glacier offshore Adélie Land (140-150°E) in summer 2000-2001
409 ranged between -0.47 and 0.05‰ (Jacobs *et al.*, 2004), equivalent to $\delta^2\text{H}$ values of 6.9 to 11.2‰
410 (average = 9‰) following the GMWL. Thus, the two major hydrogen source pools (RIS glacial ice and
411 ocean water) have highly contrasting isotope values, meaning inputs of upstream glacial ice could have a
412 large effect on surface water $\delta^2\text{H}$ values in the Adélie Land region.

413

414 Taking the average glacial meltwater $\delta^2\text{H}$ value as -275‰ and the average modern Adélie surface water
415 $\delta^2\text{H}$ value of 9‰ as end-members, and assuming a biosynthetic offset between the FA and sea water of
416 173‰ (see below), we can use a simple mixing model to estimate the percentage of glacial meltwater
417 required in the surface waters to change the $\delta^2\text{H}_{\text{FA}}$ value to those recorded in U1357B samples. The
418 most negative values occur during the early Holocene, 11.4 – 8.2 ka, averaging -214.2‰ (n=18) which,
419 converted to a surface water value of -41‰, requires 17.6% of the surface water to be comprised of
420 glacial meltwater. During this time, we argue that large volumes of meltwater were reaching the core
421 site as local glaciers retreated, leading to intense surface-water stratification. Thus, a relatively high
422 percentage of meltwater in the Adélie Land surface waters seems reasonable. During the mid-Holocene
423 (5-4 ka), the average $\delta^2\text{H}_{\text{FA}}$ is very similar (-213.9‰, n=7), requiring 17.2% of the surface water to be
424 derived from glacial meltwater. During this time, we argue for the dominant meltwater source as coming



425 from the Ross Sea, and interpret this as a major period of glacial retreat (see section 5.2), during which
426 large volumes of meltwater are injected into the surface water and transported to the Adélie coast. In
427 contrast, the most recent samples (last 0.5 ka, n=7), which includes the most positive value of the record,
428 has an average $\delta^2\text{H}_{\text{FA}}$ value of -174.5‰. This brings the surface water value up to -1.5‰, which
429 approaches modern measured values, and requires just 3.7% (e.g. well within uncertainties) of the
430 surface waters in the Adélie Land to be glacial meltwater. However, it is also possible that the meltwater
431 was dominated by more LGM-aged ice. In either case, perturbation of the exact isotopic values still
432 indicate only significant changes in the flux of glacial meltwater can account for this signal. For
433 example, the use of -330‰ (LGM values) for the ice input gives an estimate of 3% of the surface water
434 being comprised of glacial meltwater for latest Holocene values, and 14.7% for pre 8 ka values. Taking -
435 240‰ (Holocene values) for the ice input gives an estimate of 4% for latest Holocene values, and 20%
436 for pre 8 ka values). Thus even with changing isotopic values though the deglacial, this signal of
437 changing meltwater flux would still dominate. We note these are semi-quantitative estimates, as the
438 salinity and temperature fractionation could reduce these estimates further (but cannot account for the
439 whole signal).

440

441 Surface water $\delta^{18}\text{O}$ values around Antarctica (below 60°S), measured between 1964 and 2006, ranged
442 from -8.52‰ to 0.42‰ (Schmidt *et al.*, 1999), the most negative value having been measured proximal
443 to the George VI Ice Shelf edge, where high melt rates have been observed (Potter and Paren, 1985). If
444 converted to $\delta^2\text{H}$ using the global meteoric water line, these values give a $\delta^2\text{H}$ range of 83.4‰. Thus,
445 our absolute $\delta^2\text{H}_{\text{FA}}$ range of 123‰ over the Holocene suggests a range of isotopically depleted
446 meltwater inputs to our core site over this time that are 1.5 times greater than that occurring in different
447 locations around the Antarctic in recent decades. This seems plausible seen as geological evidence
448 indicates large glacial retreat and ice mass loss occurred from the Ross Sea sector during the Holocene
449 (McKay *et al.*, 2016), meaning resultant changes in surface water are likely to be greater in magnitude
450 than observed around the Antarctic in recent decades. This assumes a relatively constant value for the
451 isotopic composition of glacial meltwater, however, there is likely to be some variability due to the
452 possibility of melting ice of different $\delta^2\text{H}$ values. But, as discussed above, the meltwater is best
453 represented by the average values of the ice sheet, rather than extreme values, since it must (over the
454 broad expanse of the RIS) include an integrated signal, and thus the actual variation in meltwater $\delta^2\text{H}$
455 will be significantly within the range of the end-members.



456

457 Although the biosynthetic fractionation of the C₁₈ FAs in U1357B is unknown, we assume that the offset
458 with surface water remains relatively constant throughout the record. Sessions *et al.* (1999) showed the
459 biosynthetic fractionation of hydrogen isotopes in the C₁₈ FA from four different marine algae to range
460 from -189 to -157‰. If we take the average of these values of 173‰ and apply this as a biosynthetic
461 offset to the youngest samples in U1357B (last 0.5 ka, n=7), which includes the most positive value of
462 the record, gives an average $\delta^2\text{H}_{\text{FA}}$ value of -174.5‰. This brings the surface water value up to -1.5‰,
463 which approaches modern measured values (Jacobs *et al.*, 2004).

464

465 Furthermore, it is interesting to note that the biosynthetic offsets measured by Sessions *et al.* (1999) for
466 the C₁₈ FA from different algal species have a total $\delta^2\text{H}$ range of 32‰. Although we cannot dismiss
467 changes in the relative contribution of C₁₈ from different species in U1357B samples (and thus different
468 biosynthetic fractionations), we argue this would only be a minor control on $\delta^2\text{H}$ compared to other
469 influences. As a thought experiment, taking the above end-members for biosynthetic fractionation from
470 Sessions *et al.* (1999), even with a 100% change in C₁₈ producer to a different algal source, this could
471 only explain a quarter of the observed $\delta^2\text{H}$ change (i.e. 32‰ of 123‰).

472

473 Therefore, we interpret the first order control on $\delta^2\text{H}_{\text{FA}}$ at Site U1357 as inputs of isotopically depleted
474 glacial meltwater. Such inputs are, in turn, influenced by the mass balance of the proximal or up-current
475 glaciers and ice-shelves.

476

477 5. DISCUSSION

478

479 The stratigraphy of U1357B is divided into three units: the lowermost 10 cm recovered Last Glacial
480 Maximum (LGM) till (Unit III), overlain by 15 m of laminated mud-rich diatom oozes with ice rafted
481 debris (IRD) (Unit II), and the upper most 171 m (Unit I) consists of laminated diatom ooze with a
482 general lack of IRD and a significant reduction in terrigenous sediment (Escutia *et al.*, 2011). The
483 sedimentology and geometry of the drift prior to ~11.4 ka (Unit II) is consistent with the calving bay
484 reentrant model (Domack *et al.*, 2006; Leventer *et al.*, 2006) (Fig. 1 and Supplementary Fig. S5;
485 Supplementary Materials), whereby LGM ice retreated in the deeper troughs while remaining grounded
486 on shallower banks and ridges. Sediment laden meltwater and IRD content in Unit II (>11.4 ka) is thus



487 likely derived from local outlet glaciers. However, anomalously old radiocarbon ages due to glacial
488 reworking precludes development of a reliable age model prior to the Holocene (Supplementary
489 Materials).

490

491 **5.1 Early Holocene**

492 The base of the drift deposit shows downlapping of material suggesting a supply from the south,
493 indicating local focusing of meltwater and terrigenous material was the dominating influence until 11.4
494 ka (Supplementary Materials). This is overlain by onlapping strata (Unit I) with the drift forming an
495 east-west elongation on the northern flank of the Dumont d'Urville Trough, which is more consistent
496 with advection of material from the east than with delivery from local outlet glaciers to the south. Thus,
497 an increased meltwater influence from the Ross Sea is likely since this time (Supplementary Materials).

498

499 Due to the potential for competing sources of glacial meltwater in the earliest Holocene, we focus our
500 study on Unit I, where there is less influence of calving bay processes (Escutia *et al.*, 2011). However,
501 the earliest part of Unit I (11.4 to 8 ka BP), which includes the most negative $\delta^2\text{H}_{\text{FA}}$ values, is
502 characterized by a very gradual upcore increase of sorting in the terrigenous sediment supply, decreasing
503 natural gamma ray (NGR) values (Supplementary Fig. S4) and a general lack of IRD. We conservatively
504 interpret this as potentially maintaining some local glacial meltwater input from local outlet glaciers in
505 the lowermost interval of Unit I. Nevertheless, this process was probably greatly reduced relative to Unit
506 II deposition and it is likely much of this signal between 11.4 and 8 ka could still be derived from water
507 masses advecting to the site from the east (e.g. the Ross Sea).

508

509 This is supported by geological and cosmogenic evidence which demonstrates that the Wilkes Land
510 margin of the East Antarctic, and also the Amundsen Sea margins, had retreated to their modern-day
511 positions by ~10 ka (Bentley *et al.*, 2014; Mackintosh *et al.*, 2014; Hillenbrand *et al.*, 2017);
512 Supplementary Materials), thus these margins are unlikely to contribute large scale shifts in meltwater
513 fluxes to the Adélie Coast during most of the Holocene. Glacial retreat, however, persisted in the Ross
514 Sea until at least 3 ka (Anderson *et al.*, 2014; Spector *et al.*, 2017) (Supplementary Materials) providing
515 a large upstream source of meltwater feeding into the Adélie Coast. We therefore interpret our meltwater
516 signal as being dominated by Ross Sea inputs since at least 8 ka, but potentially as early as 11.4 ka.
517 Furthermore, the retreat of grounded ice from the outer Ross Sea continental shelf was accompanied by



518 the growth of a significant floating ice shelf (which was not the case in the Amundsen Sea or proximal
519 East Antarctic coast) (Bentley *et al.*, 2014).

520

521 An overall trend to more positive $\delta^2\text{H}_{\text{FA}}$ values, from the most negative value of the record at ~9.6 ka, to
522 ~8 ka indicates decreasing meltwater (Fig. 2a), thus suggesting a gradually diminished input from either
523 local outlet glaciers or the Ross Sea. This is associated with an increase in MARs, between 10 and 8 ka,
524 and is tentatively interpreted to represent the final retreat of residual ice from local bathymetric highs
525 allowing more material to advect into the drift (Supplementary Fig. S4). Although there is millennial
526 scale variability, MARs remain relatively high until 4.5 ka. However, $\delta^2\text{H}_{\text{FA}}$ and MARs show greater
527 coherence at the millennial-scale after 7 ka BP, suggesting that increased fluxes of glacial meltwater
528 broadly corresponded to stronger easterly currents, which advected biogenic and terrigenous material
529 into the drift.

530

531 **5.2 Middle Holocene**

532 A negative excursion in $\delta^2\text{H}_{\text{FA}}$ starting from 6 ka and culminating at 4.5 ka is interpreted to record a
533 period of enhanced glacial meltwater flux to the site relating to a final retreat phase of the major ice
534 sheet grounding line in the Ross Sea embayment (Fig. 5). A marked enrichment of Ba/Ti ratios also
535 occurs at 4.5 ka, reaching values of 36.1, on a background of baseline fluctuations between 0.1 and 2.7
536 (Fig. 2g), which suggests enhanced primary productivity, potentially driven by meltwater-induced
537 stratification. Ongoing Holocene retreat in the Ross Sea is interpreted to be primarily the consequence of
538 marine ice sheet instability processes resulting from the overdeepened continental shelf in that sector
539 (McKay *et al.*, 2016).

540

541 The $\delta^2\text{H}_{\text{FA}}$ peak at 4.5 ka in U1357 coincides directly with a rapid shift in HBI biomarker ratios at the
542 site, as well as sea ice proxies recorded in nearby site MD03-2601, in the Ross embayment (Taylor
543 Dome ice core on a revised age model) (Steig *et al.*, 1998; Baggenstos *et al.*, 2018) and Prydz Bay
544 (JPC24) (Denis *et al.*, 2010) (Fig. 2), reflecting a widespread increase in coastal sea-ice concentration
545 and duration. We interpret decreasing MAR and finer-grained terrigenous content (e.g. increased mud
546 percent) at Site U1357 after 4.5 ka (Supplementary Fig. S4) to also be a consequence of increased
547 coastal sea ice, reducing wind stress on the ocean surface and limiting the easterly advection of detritus
548 to the drift deposit.



549

550 Coastal sea-ice concentration and duration remain high throughout the rest of the Holocene (this study
551 and Steig *et al.*, 1998; Crosta *et al.*, 2008; Denis *et al.*, 2010), compared to the period before 4.5 ka,
552 despite a decrease in glacial meltwater flux to the U1357 site. In addition, meltwater input prior to 4.5 ka
553 does not have a major influence on sea ice extent. Thus, an increase in meltwater flux cannot explain the
554 Neoglacial intensification of sea ice at ~4.5 ka. Here, we propose that greater coastal sea ice cover since
555 4.5 ka is related to the development of a large ice-shelf cavity in the Ross Sea as the ice sheet retreats
556 (Fig. 5), which pervasively modified ice shelf-ocean interactions and increased sea ice production.
557 Models suggest a large cavity on the continental shelf increases contact between basal-ice and
558 circulating ocean water, driving the formation of a cool, fresh water mass feeding into the AASW,
559 stabilizing the water column and enhancing the production of sea ice (Hellmer, 2004) (Fig. 5). However,
560 under small cavities such as in the modern Amundsen Sea influenced by warm-water incursions, ice
561 shelf melting results in an “ice pump” enhancement of sub-ice shelf circulation. This increases flow of
562 warm Circumpolar Deep Water (CDW) under the ice shelf that is 100-500 times the rate of melt, and
563 this volume of water does not allow for supercooling. Small cavity ice shelf outflows are therefore warm
564 and act to restrict sea ice at the ice shelf front (Jourdain *et al.*, 2017). Thus, during the Holocene, the size
565 of the cavity must have reached a threshold after which this positive warming feedback switched to a
566 negative feedback. We argue that such a tipping point takes place at 4.5 ka BP, when our proxy data
567 suggest meltwater peaks, and would explain why the increase in sea-ice concentration appears rapid and
568 only occurs at the peak of the meltwater input, and not during its prior increase, or previous meltwater
569 inputs (Fig. 2a-g).

570

571 Although the glacial meltwater volume is greatly reduced after 4.5 ka BP, the volume of Ice Shelf Water
572 (ISW) produced beneath the modern RIS is estimated at 0.86 Sv-1.6 Sv (Holland *et al.*, 2003; Smethie
573 and Jacobs, 2005). We note that ISW is not glacial meltwater, but it is defined as a supercooled water
574 mass formed through interaction with the base of the RIS, but once formed acts to modify other water
575 masses in the Ross Sea. A significant proportion of ISW is high salinity and is thus advected northwards
576 at intermediate waters depth to ultimately form AABW. However, a significant volume of ISW is lower
577 salinity and buoyant, due to development of frazil ice, and acts to mixes with surface waters (Robinson
578 *et al.*, 2014). Currently, a 0.4 Sv plume of ISW in the western margin of the Ross Ice Shelf (Robinson *et al.*
579 *et al.*, 2014) is directly delivered to the surface resulting in enhanced sea ice production, while seasonal



580 melt of this enhanced sea ice further acts to cool and freshen surface waters. Although unrealistic in the
581 context of a post-LGM meltwater flux from the Ross Sea alone, the larger meltwater release scenarios in
582 our simulations (0.5 to 1 Sv) show the potential pathways that a cool, fresher surface water mass
583 collecting and forming on the broad Ross Sea continental shelf would follow (Fig. 3). These waters are
584 transported in easterly coastal currents to the Weddell Sea and the Antarctic Peninsula. This eventually
585 retroflects to join the Antarctic Circumpolar Current (Fig. 3b), and thus has potential for cooling and
586 freshening in the South Atlantic far offshore, as the ice shelf cavity increased in the Ross Sea. Indeed,
587 offshore site ODP 1094 records increased lithics in the South Atlantic after 4.5 ka (Fig. 2f), relative to
588 the period before, suggested to have been predominantly transported by sea ice indicating a cooling in
589 sea surface temperatures and increase in sea-ice extent in the South Atlantic at this time (Nielsen *et al.*,
590 2007). However, it also is feasible that this circum-Antarctic cooling signal indicates similar melt
591 processes may have been occurring in the Weddell Sea at ~4.5 ka, as suggested by cosmogenic nuclide
592 data (Hein *et al.*, 2016).

593

594 **5.3 What Drove the Neoglacial Transition?**

595 Our observed coastal sea-ice increase is part of a widespread transition to Neoglacial conditions both
596 globally and at high southern latitudes (Kim *et al.*, 2002; Masson-Delmotte *et al.*, 2011; Marcott *et al.*,
597 2013; Solomina *et al.*, 2015). However, most current climate models do not simulate this cooling trend,
598 resulting in a significant data-model mismatch (Liu *et al.*, 2014) (Supplementary Fig. S7). Marine ice
599 sheet retreat along the entire Pacific margin of West Antarctic has previously been proposed to be
600 triggered by enhanced wind-driven incursions of warm CDW onto the continental shelves in the early
601 Holocene (Hillenbrand *et al.*, 2017), with continued retreat in the Ross Sea being the consequence of the
602 overdeepened continental shelf and marine ice sheet instability processes (McKay *et al.*, 2016).
603 However, we propose that a series of negative feedbacks associated with this retreat and RIS cavity
604 expansion occurred in the mid-Holocene, with similar processes possibly occurring in the Weddell Sea,
605 leading to the onset and continuation of Neoglacial conditions. Widespread albedo changes associated
606 with increased coastal sea ice would have amplified regional cooling trends (Masson-Delmotte *et al.*,
607 2011), whilst increased stratification resulting from seasonal sea-ice melt and increased ISW production
608 drove the deepening of the fresher water surface isopycnal at the continental shelf break. Grounding line
609 retreat creates new space for continental shelf water masses to form, while ice shelf cavity expansion
610 promotes supercooling and freshening of AASW. Thus, as seasonal sea ice melt and ice shelf



611 supercooling processes played a greater role in enhancing AASW production on the continental shelf,
612 they would have acted to restrict warmer subsurface water transport onto the continental shelf (Smith Jr.
613 *et al.*, 2012) (Fig. 5). Furthermore, the Neoglacial sea-ice increase itself may have been associated with
614 a stabilising feedback mechanism (which also is not resolved in ice-ocean models) through its role in
615 dampening ocean-induced wave flexural stresses at ice shelf margins, reducing their vulnerability to
616 catastrophic collapse (Massom *et al.*, 2018). We suggest that some combination of the above processes
617 slowed the rate of Ross Sea grounding line retreat (Supplementary Materials) and reduced basal ice shelf
618 melt as indicated by a trend towards more positive $\delta^2\text{H}_{\text{FA}}$ values in U1357 between 4.5 and 3 ka (Fig.
619 2a). Furthermore, large Antarctic ice shelves currently have large zones of marine accreted ice resulting
620 from supercooling (Rignot *et al.*, 2013), thus the signature of $\delta^2\text{H}_{\text{FA}}$ is anticipated to become more
621 positive as the ice shelf approaches a steady state of mass balance, relative to the thinning phases when
622 basal melt rates exceed that of accretion. The stabilization of $\delta^2\text{H}_{\text{FA}}$ values observed at 3 ka in U1357
623 suggests the Ross Ice Shelf has maintained a relatively steady state of mass balance since this time.

624

625 A recent study implies an increase in katabatic winds since at least 3.6 ka in the Ross Sea (Mezgec *et al.*,
626 2017) (Supplementary Materials), leading to enhanced polynya activity. During colder Antarctic
627 climates, increased latitudinal temperature gradients enhanced katabatic winds in the Ross Sea (Rhodes
628 *et al.*, 2012). We interpret this katabatic wind and polynya activity signal to be a response to the
629 preceding Neoglacial cooling at 4.5 ka and evolution of the modern ocean-ice shelf connectivity, which
630 our data suggest was primarily driven by ice shelf cavity expansion. Furthermore, this transition takes
631 place on the background of declining winter insolation (Berger and Loutre, 1991) which would have
632 acted to further enhance and maintain these changes. This insolation decline has previously been
633 hypothesised as a driver of the Neoglacial increase in coastal sea ice (Denis *et al.*, 2010), however this
634 monotonic decrease contrasts with the markedly rapid increase in sea ice observed in many records (Fig
635 2). Our mechanism of ice shelf cavity expansion, reaching a threshold that promoted significant
636 supercooling of continental shelf water masses, reconciles both the rapidity and timing of Neoglacial
637 onset in the middle Holocene.

638

639 **6. Conclusions and Implications for Antarctic Climate, Sea-Ice and Ice Shelf Behaviour**

640 The lack of these coupled ice-ocean processes is apparent in recent Earth system model experiments, in
641 particular the incorporation of evolving ice shelf cavities, with Trace-21k for example, instead



642 simulating a decrease in Antarctic sea-ice extent and thickness after 5 ka (Supplementary Fig. S7).
643 These model outputs are in direct contrast to multiple lines of proxy data in this study and previous work
644 (Steig *et al.*, 1998; Crosta *et al.*, 2008; Denis *et al.*, 2010). Consequently, our results provide insights
645 into the magnitude of this data-model mismatch, as well as a mechanism for rapid sea-ice change and
646 grounding line stabilisation on the background of a warming climate (Liu *et al.*, 2014), both on modern
647 and Holocene time scales. Better representation of the role of evolving ice shelf cavities on oceanic
648 water mass evolution and sea-ice dynamics, which our data indicate acted as a strong negative feedback,
649 will be fundamental to understanding the oceanographic and glaciological implications of future ice
650 shelf loss in the Antarctic.

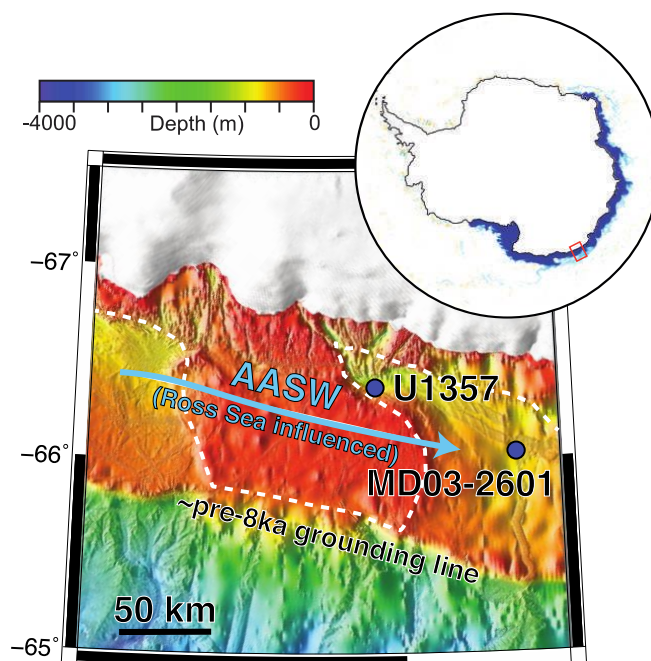
651

652

653 **Figures**

654

655

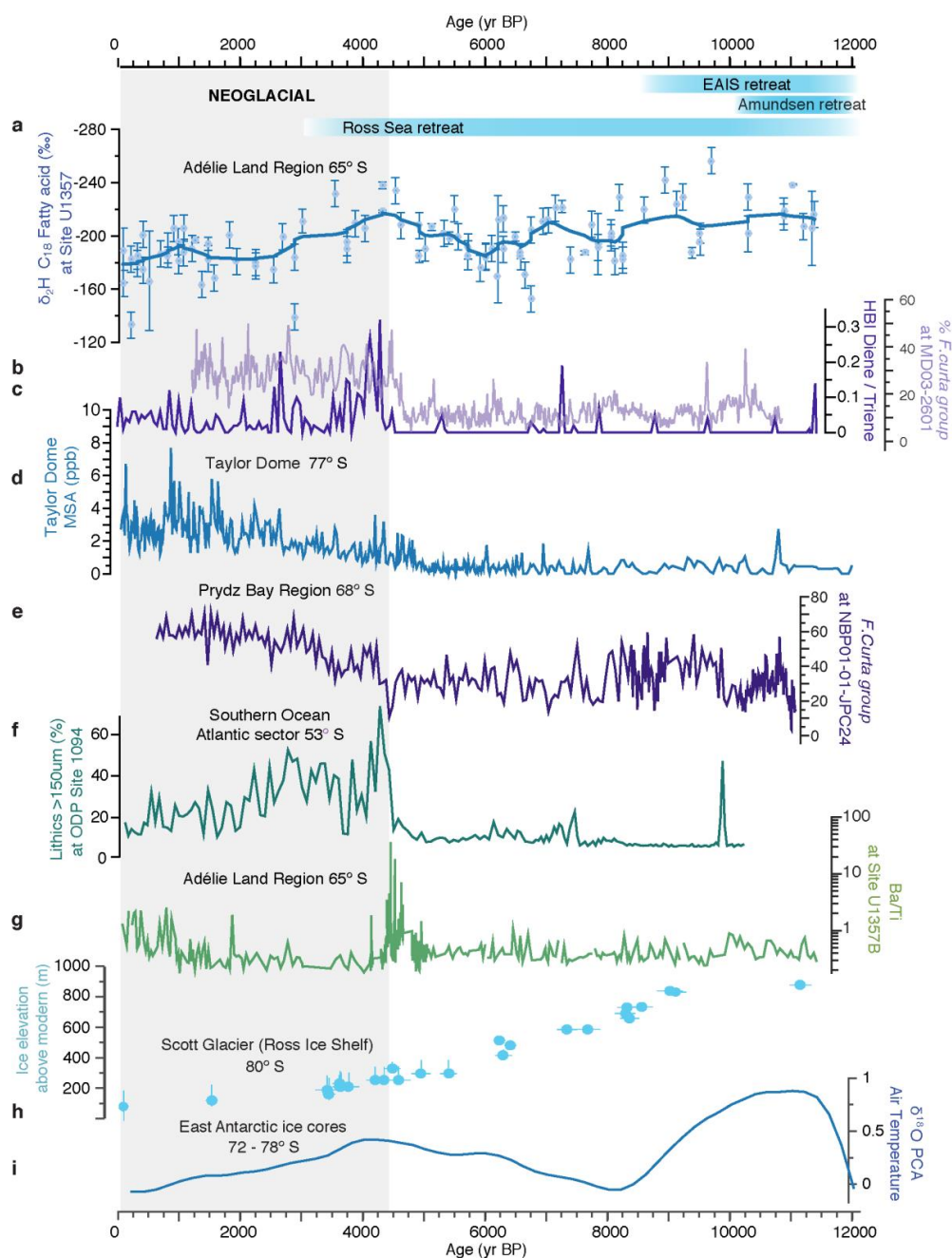


656

657 **Figure 1: Location of Sites U1357 and MD03-2601 (blue dots).** The ice sheet grounding line formed a



658 calving-bay environment (dashed white line) prior to 11.4 ka, but since at least 8.2 ka Antarctic Surface
659 Water flow is largely advected from the Ross Sea (blue line). Inset map: pathway of freshwater (dark
660 blue) after 1 year of 1 Sv meltwater released from along the edge of the Ross Ice Shelf in a model
661 simulation (Supplementary Materials).
662



663 **Figure 2: Holocene Adélie Land proxy records from IODP Site U1357 and other circum-Antarctic**
 664 **sites.** Glacial retreat chronologies are shown as bars at the top as discussed in the text. a) $\delta^2\text{H}$ C_{18} fatty
 665 acid at Site U1357 (errors bars based on replicates), with robust locally weighted smoothing (rlowss). b)



666 *Fragilariopsis curta* group (*F. curta* and *F. cylindrus*) relative abundance at MD03-2601, as a proxy of
667 sea-ice conditions (Crosta *et al.*, 2008) c) di-unsaturated HBI (C_{25:2}; Diene)/tri-unsaturated HBI isomer
668 (C_{25:3}; Triene) ratio at Site U1357 d) Methanesulfonate (MSA) concentrations (ppb) from Taylor Dome
669 ice core e) *F. curta* group relative abundances in core NBP-01-JPC24 f) Coarse lithic (ice-rafted)
670 content at ODP 1094 (Nielsen *et al.*, 2007) g) Ba/Ti (logarithmic scale) at Site U1357 h) ¹⁰Be
671 cosmogenic nuclide ages from Scott Glacier in the SW Ross Ice Shelf region (Spector *et al.*, 2017) i)
672 Temperature signal from principal component analyses of five δ¹⁸O records in five East Antarctic ice
673 cores (Vostok, EPICA Dome C, EPICA Dronning Maud Land, Dome Fuji and Talos Dome) (Masson-
674 Delmotte *et al.*, 2011).

675

676

677

678

679

680

681

682

683

684

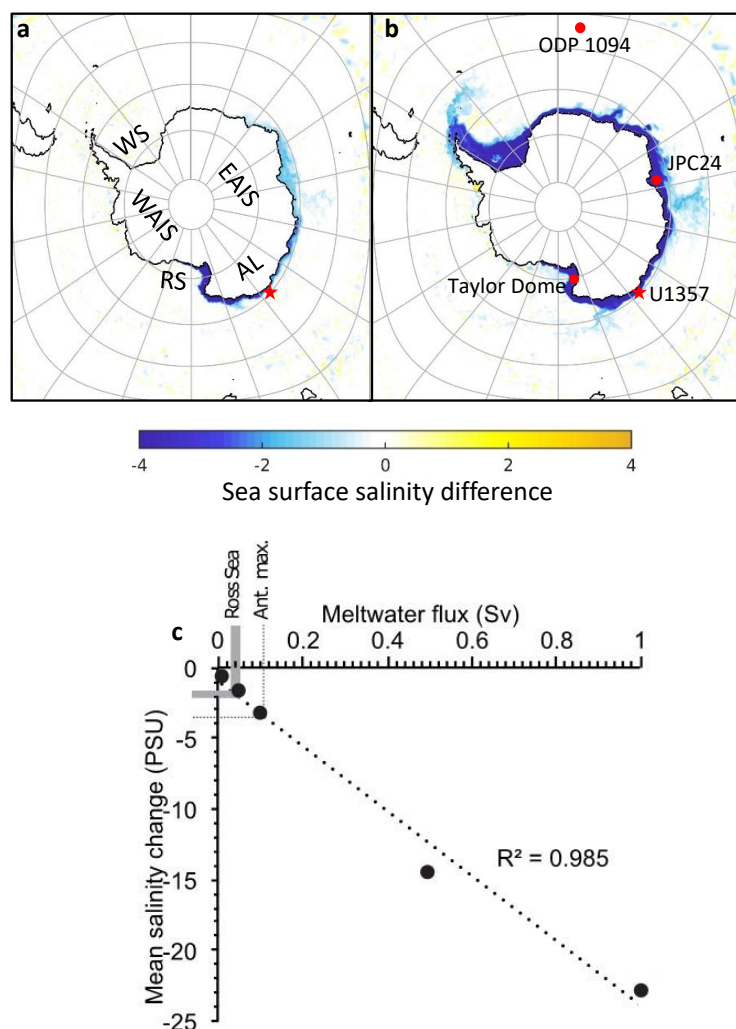
685

686

687



688



689 **Figure 3: MITgcm simulations of meltwater release from along the edge of the Ross Ice Shelf.** First
690 two images show sea-surface salinity difference (in practical salinity units) after 3.5 model years
691 resulting from meltwater release volumes of a) 0.1 Sv and b) 0.5 Sv. Red star indicates position of Site
692 U1357 (this study) and red dots show positions of other core sites mentioned in this study where a Mid
693 Holocene increase in sea ice and/or cooling is recorded: Taylor Dome (Steig *et al.*, 1998; Baggenstos
694 *et al.*, 2018), JPC24 (Denis *et al.*, 2010) and ODP 1094 (Nielsen *et al.*, 2007). AL = Adélie Land, RS =
695 Ross Sea, WS = Weddell Sea, EAIS = East Antarctic Ice Sheet, WAIS = West Antarctic Ice Sheet. c)
696 Scatter plot of simulated meltwater flux (Sv) against mean salinity difference at U1357 core site. Grey



697 band indicates range of plausible Holocene to deglacial Ross Sea meltwater inputs. Dotted line indicates
698 maximum Antarctic meltwater during the Holocene.

699

700

701

702

703

704

705

706

707

708

709

710

711

712

713

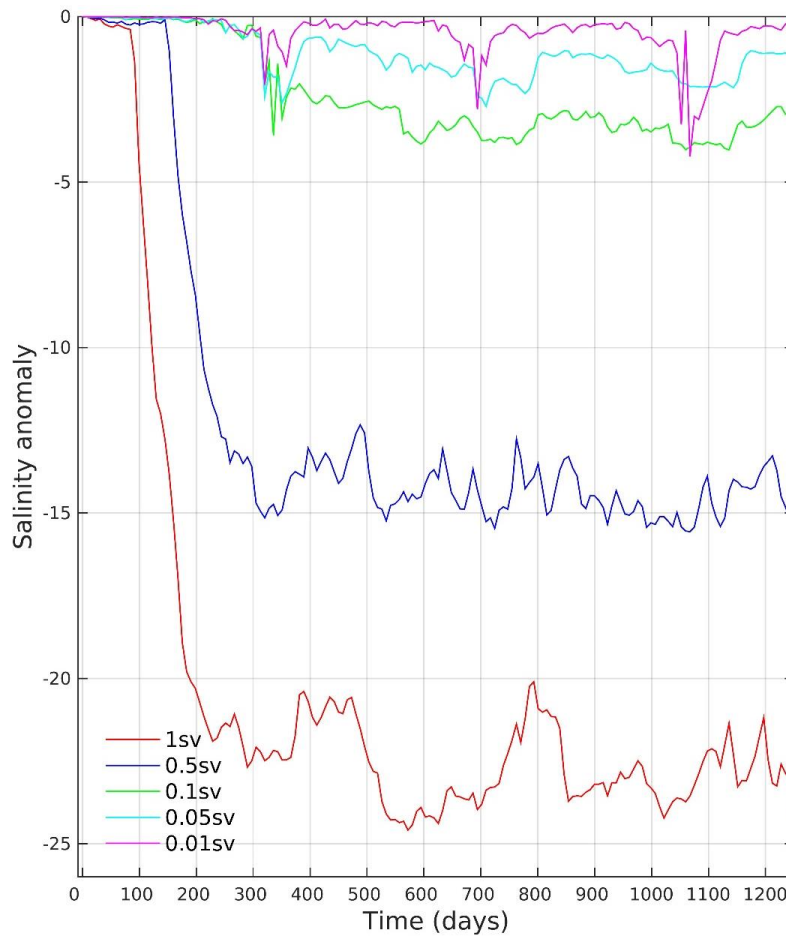
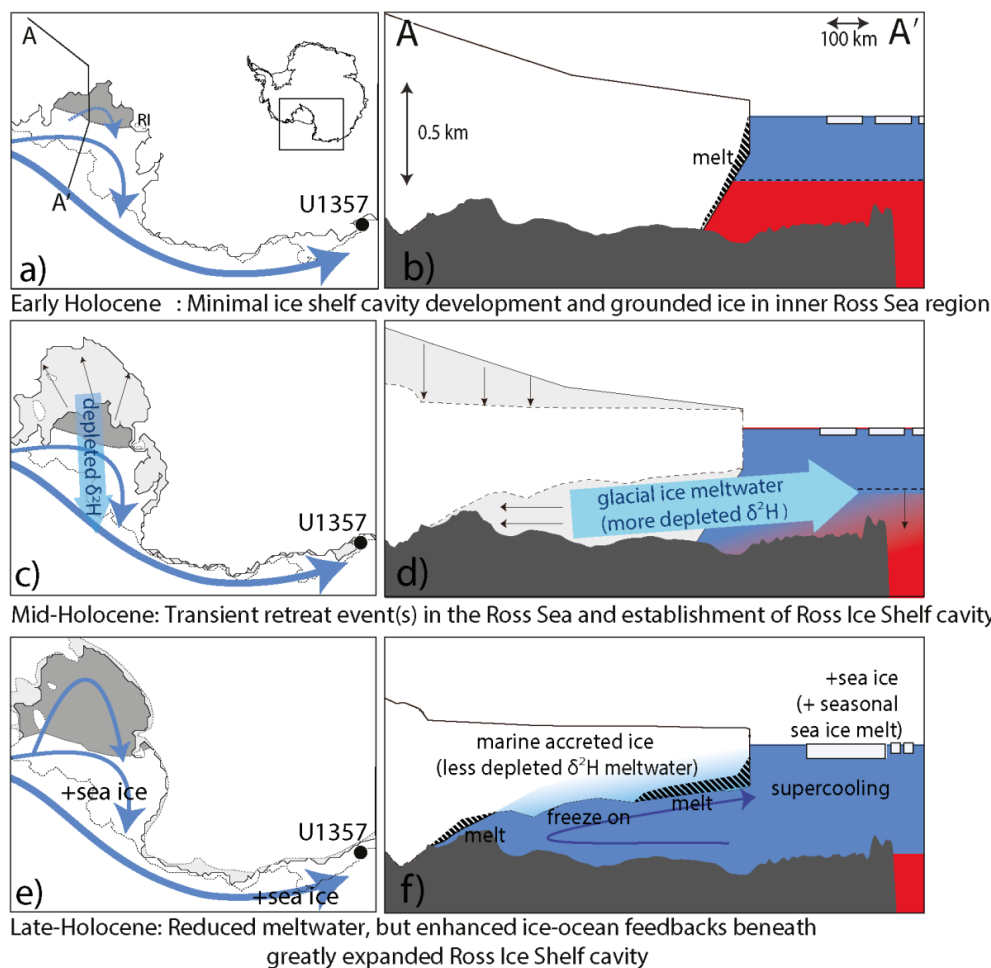


Figure 4 Simulated salinity anomalies over time at Site U1357 for the five meltwater release experiments.



714

715 **Figure 5: Conceptual model of evolving Holocene glacial and oceanographic conditions in the Ross**

716 **Sea region.** Panels on the left show modelled grounding line positions (McKay *et al.*, 2016), and

717 proposed circulation of surface and sub-ice shelf circulating waters (light blue arrows). Panels on the

718 right show cross sections of the Ross Ice Shelf (RIS) and ice-ocean interactions. Dark blue = cool

719 surface waters, Red = warm subsurface waters. a) The grounding line in Adélie Land is near its modern

720 location, but near Ross Island (RI) in the Ross Sea, and ice shelf cavity (dark grey shading) is reduced in

721 size relative to today (McKay *et al.*, 2016). b) Continental shelf profile A-A' (panel a) shows a Ross Sea

722 grounding line in a mid-continental shelf location in close proximity to the RIS calving line (McKay *et*

723 *al.*, 2016), with subsurface warming on the continental shelf triggering WAIS deglaciation (Hillenbrand

724 *et al.*, 2017). c) Most grounding line retreat south of RI occurred between 9 and 4.5 ka (light grey



725 shading with black arrows represents area of retreat over this period), proposed to be the consequence of
726 marine ice sheet instability, but the ice shelf calving line remained near its present position (McKay *et*
727 *al.*, 2016; Spector *et al.*, 2017). d) Grounding line retreat and ice shelf thinning released meltwater with
728 negative $\delta^2\text{H}$ into the surface waters. Increasing ice shelf-oceanic interactions with the development of
729 the ice shelf cavity (dark grey) led to enhanced Antarctic Surface Water formation; f) Minimal
730 grounding line retreat has occurred since 4.5 ka, and the RIS supercools AASW leading to enhanced
731 sea-ice formation despite reduced glacial meltwater flux. Seasonal sea ice meltwater further freshens and
732 cools AASW. Increased production of AASW on the continental shelf leads to isopycnal deepening
733 (dotted line) and limits flow onto the continental shelf slowing further grounding line retreat. However,
734 as the ice shelf is near steady state mass balance and there is a component of marine accreted ice at the
735 base of the ice shelf (Rignot *et al.*, 2013), the strength of the $\delta^2\text{H}$ signal is reduced relative to periods of
736 mass balance loss.

737

738

739 **References:**

740

741 Adcroft, A. *et al.* (2004) ‘Implementation of an Atmosphere–Ocean General Circulation Model on the
742 Expanded Spherical Cube’, *Monthly Weather Review*, 132(12), pp. 2845–2863. doi:
743 10.1175/MWR2823.1.

744 Anderson, J. B. *et al.* (2014) ‘Ross Sea paleo-ice sheet drainage and deglacial history during and since
745 the LGM’, *Quaternary Science Reviews*. Elsevier Ltd, 100, pp. 31–54. doi:
746 10.1016/j.quascirev.2013.08.020.

747 Aoki, S. *et al.* (2013) ‘Widespread freshening in the Seasonal Ice Zone near 140°E off the Adélie Land
748 Coast, Antarctica, from 1994 to 2012’, *Journal of Geophysical Research: Oceans*, 118(11), pp. 6046–
749 6063. doi: 10.1002/2013JC009009.

750 Arrigo, K. R. and van Dijken, G. L. (2003) ‘Phytoplankton dynamics within 37 Antarctic coastal
751 polynya systems’, *Journal of Geophysical Research*, 108(C8), p. 3271. doi: 10.1029/2002JC001739.

752 Asper, V. L. and Smith, W. O. (1999) ‘Particle fluxes during austral spring and summer in the southern
753 Ross Sea, Antarctica’, *Journal of Geophysical Research: Oceans*, 104(C3), pp. 5345–5359. doi:
754 10.1029/1998JC900067.

755 Baggenstos, D. *et al.* (2018) ‘A Horizontal Ice Core From Taylor Glacier, Its Implications for Antarctic
756 Climate History, and an Improved Taylor Dome Ice Core Time Scale’, *Paleoceanography and*
757 *Paleoclimatology*, 33(7), pp. 778–794. doi: 10.1029/2017PA003297.



- 758 Beans, C. *et al.* (2008) ‘A study of the diatom-dominated microplankton summer assemblages in coastal
759 waters from Terre Adelie to the Mertz Glacier, East Antarctica (139°E-145°E)’, *Polar Biology*, 31(9),
760 pp. 1101–1117. doi: 10.1007/s00300-008-0452-x.
- 761 Belt, S. T. *et al.* (2007) ‘A novel chemical fossil of palaeo sea ice: IP25’, *Organic Geochemistry*, 38(1),
762 pp. 16–27. doi: 10.1016/j.orggeochem.2006.09.013.
- 763 Bentley, M. J. *et al.* (2014) ‘A community-based geological reconstruction of Antarctic Ice Sheet
764 deglaciation since the Last Glacial Maximum’, *Quaternary Science Reviews*, 100, pp. 1–9. doi:
765 10.1016/j.quascirev.2014.06.025.
- 766 Berger, A. and Loutre, M. F. (1991) ‘Insolation values for the climate of the last 10 million years’,
767 *Quaternary Science Reviews*, 10(4), pp. 297–317. doi: 10.1016/0277-3791(91)90033-Q.
- 768 Bindoff, N., Rintoul, S. and Massom, R. (2000) ‘Bottom water formation and polynyas in Adelie Land,
769 Antarctica’, *Papers and Proceedings of the Royal Society of Tasmania*, 133(3), pp. 51–56. doi:
770 10.26749/rstpp.133.3.51.
- 771 Brook, E. J. *et al.* (2005) ‘Timing of millennial-scale climate change at Siple Dome, West Antarctica,
772 during the last glacial period’, *Quaternary Science Reviews*, 24(12–13), pp. 1333–1343. doi:
773 10.1016/j.quascirev.2005.02.002.
- 774 Budge, S. M. *et al.* (2008) ‘Tracing carbon flow in an arctic marine food web using fatty acid-stable
775 isotope analysis’, *Oecologia*, 157(1), pp. 117–129. doi: 10.1007/s00442-008-1053-7.
- 776 Campagne, P. *et al.* (2015) ‘Glacial ice and atmospheric forcing on the Mertz Glacier Polynya over the
777 past 250 years’, *Nature Communications*, 6. doi: 10.1038/ncomms7642.
- 778 Condron, A. and Winsor, P. (2012) ‘Meltwater routing and the Younger Dryas’, *Proceedings of the
779 National Academy of Sciences*, 109(49), pp. 19928–19933. doi: 10.1073/pnas.1207381109.
- 780 Crosta, X., Denis, D. and Ther, O. (2008) ‘Sea ice seasonality during the Holocene, Adelie Land, East
781 Antarctica’, *Marine Micropaleontology*, 66(3–4), pp. 222–232. doi: 10.1016/j.marmicro.2007.10.001.
- 782 Dalsgaard, J. *et al.* (2003) ‘Fatty acid trophic markers in the pelagic marine environment’, *Advances in
783 Marine Biology*, 46, pp. 225–340. doi: 10.1016/S0065-2881(03)46005-7.
- 784 DeMaster, D. J. (1981) ‘The supply and accumulation of silica in the marine environment’, *Geochimica
785 et Cosmochimica Acta*, 45(10), pp. 1715–1732. doi: 10.1016/0016-7037(81)90006-5.
- 786 Denis, D. *et al.* (2010) ‘Sea ice and wind variability during the Holocene in East Antarctica: Insight on
787 middle-high latitude coupling’, *Quaternary Science Reviews*, 29(27–28), pp. 3709–3719. doi:
788 10.1016/j.quascirev.2010.08.007.
- 789 DiTullio, G. R. *et al.* (2000) ‘Rapid and early export of *Phaeocystis antarctica* blooms in the Ross Sea,
790 Antarctica’, *Nature*, 404(6778), pp. 595–598. doi: 10.1038/35007061.
- 791 Domack, E. *et al.* (2006) ‘Subglacial morphology and glacial evolution of the Palmer deep outlet



- 792 system, Antarctic Peninsula’, *Geomorphology*, 75(1–2 SPEC. ISS.), pp. 125–142. doi:
793 10.1016/j.geomorph.2004.06.013.
- 794 Escutia, C. *et al.* (2011) ‘Expedition 318 summary’, in. doi: 10.2204/iodp.proc.318.101.2011.
- 795 Etourneau, J. *et al.* (2013) ‘Holocene climate variations in the western Antarctic Peninsula: Evidence for
796 sea ice extent predominantly controlled by changes in insolation and ENSO variability’, *Climate of the*
797 *Past*, 9(4), pp. 1431–1446. doi: 10.5194/cp-9-1431-2013.
- 798 Feakins, S. J., Warny, S. and Lee, J.-E. (2012) ‘Hydrologic cycling over Antarctica during the middle
799 Miocene warming’, *Nature Geoscience*, 5. doi: 10.1038/NGEO1498.
- 800 Hein, A. S. *et al.* (2016) ‘Mid-Holocene pulse of thinning in the Weddell Sea sector of the West
801 Antarctic ice sheet’, *Nature Communications*. Nature Publishing Group, 7, p. 12511. doi:
802 10.1038/ncomms12511.
- 803 Hellmer, H. H. (2004) ‘Impact of Antarctic ice shelf basal melting on sea ice and deep ocean properties’,
804 *Geophysical Research Letters*, 31(10), pp. 1–4. doi: 10.1029/2004GL019506.
- 805 Hillenbrand, C. D. *et al.* (2017) ‘West Antarctic Ice Sheet retreat driven by Holocene warm water
806 incursions’, *Nature*, 547(7661), pp. 43–48. doi: 10.1038/nature22995.
- 807 Holland, D. M., Jacobs, S. S. and Jenkins, A. (2003) ‘Modelling the ocean circulation beneath the Ross
808 Ice Shelf’, *Antarctic Science*, 15(1), pp. 13–23. doi: 10.1017/S0954102003001019.
- 809 Huang, Y. *et al.* (1999) ‘Glacial-interglacial environmental changes inferred from molecular and
810 compound-specific $\delta^{13}\text{C}$ analyses of sediments from Sacred Lake, Mt. Kenya’, *Geochimica et*
811 *Cosmochimica Acta*, 63(9), pp. 1383–1404. doi: 10.1016/S0016-7037(99)00074-5.
- 812 Hughes, K. *et al.* (2014) ‘Extension of an Ice Shelf Water plume model beneath sea ice with application
813 in McMurdo Sound, Antarctica’, *Journal of Geophysical Research: Oceans*, 119, pp. 8662–8687. doi:
814 10.1002/2014JC010248. Received.
- 815 Jacobs, S. S. *et al.* (2004) *Summer Oceanographic Measurements near the Mertz Polynya (140–150E)*
816 *on NB Palmer Cruise 00–08*. doi: 10.15784/601161.
- 817 Jacobs, S. S., Giulivi, C. F. and Mele, P. A. (2002) ‘Freshening of the Ross Sea During the Late 20th
818 Century’, *Science*, 297(5580), pp. 386–389. doi: 10.1126/science.1069574.
- 819 Jensen, S., Renberg, L. and Reutergårdh, L. (1977) ‘Residue Analysis of Sediment and Sewage Sludge
820 for Organochlorines in the Presence of Elemental Sulfur’, *Analytical Chemistry*, 49(2), pp. 316–318.
821 doi: 10.1021/ac50010a033.
- 822 Johns, L. *et al.* (1999) ‘Identification of a C₂₅ highly branched isoprenoid (HBI) diene in Antarctic
823 sediments, Antarctic sea-ice diatoms and cultured diatoms’, *Organic Geochemistry*, 30(11), pp. 1471–
824 1475. doi: 10.1016/S0146-6380(99)00112-6.
- 825 Jones, J. M. *et al.* (2016) ‘Assessing recent trends in high-latitude Southern Hemisphere surface



- 826 climate', *Nature Climate Change*. Nature Publishing Group, 6(10), pp. 917–926. doi:
827 10.1038/nclimate3103.
- 828 Jourdain, N. C. *et al.* (2017) 'Ocean circulation and sea-ice thinning induced by melting ice shelves in
829 the Amundsen Sea', *Journal of Geophysical Research: Oceans*, 122(3), pp. 2550–2573. doi:
830 10.1002/2016JC012509. Received.
- 831 Killops, S. and Killops, V. (2004) *Introduction to Organic Geochemistry*, Blackwell Publishing Ltd. doi:
832 10.1002/9781118697214.
- 833 Kim, J. H. *et al.* (2002) 'Interhemispheric comparison of deglacial sea-surface temperature patterns in
834 Atlantic eastern boundary currents', *Earth and Planetary Science Letters*, 194(3–4), pp. 383–393. doi:
835 10.1016/S0012-821X(01)00545-3.
- 836 Kim, J. H. *et al.* (2010) 'New indices and calibrations derived from the distribution of crenarchaeal
837 isoprenoid tetraether lipids: Implications for past sea surface temperature reconstructions', *Geochimica
838 et Cosmochimica Acta*, 74(16), pp. 4639–4654. doi: 10.1016/j.gca.2010.05.027.
- 839 Kopczynska, E. E. *et al.* (1995) 'Phytoplankton Composition and Cell Carbon Distribution in Prydz
840 Bay, Antarctica - Relation To Organic Particulate Matter and Its Delta-C-13 Values', *Journal of
841 Plankton Research*, 17(4), pp. 685–707. doi: 10.1093/plankt/17.4.685.
- 842 Kusahara, K., Hasumi, H. and Tamura, T. (2010) 'Modeling sea ice production and dense shelf water
843 formation in coastal polynyas around East Antarctica', *Journal of Geophysical Research: Oceans*,
844 115(10), p. C10006. doi: 10.1029/2010JC006133.
- 845 Leventer, A. *et al.* (2006) 'Marine sediment record from the East Antarctic margin reveals dynamics of
846 ice sheet recession', *GSA Today*, 16(12), pp. 4–10. doi: 10.1130/GSAT01612A.1.
- 847 Liu, Z. *et al.* (2014) 'The Holocene temperature conundrum', *Proceedings of the National Academy of
848 Sciences*, 111(34), pp. E3501–E3505. doi: 10.1073/pnas.1407229111.
- 849 Mackintosh, A. N. *et al.* (2014) 'Retreat history of the East Antarctic Ice Sheet since the Last Glacial
850 Maximum', *Quaternary Science Reviews*. Elsevier Ltd, 100, pp. 10–30. doi:
851 10.1016/j.quascirev.2013.07.024.
- 852 Marcott, S. a. *et al.* (2013) 'A Reconstruction of Regional and Global Temperature for the Past 11,300
853 Years', *Science (New York, N.Y.)*, 339(6124), pp. 1198–1201. doi: 10.1126/science.1228026.
- 854 Marshall, J. *et al.* (1997) 'A finite-volume, incompressible Navier Stokes model for studies of the ocean
855 on parallel computers', *Journal of Geophysical Research: Oceans*, 102(C3), pp. 5753–5766. doi:
856 10.1029/96JC02775.
- 857 Marsland, S. J. *et al.* (2004) 'Modeling water mass formation in the Mertz Glacier Polynya and Ad??lie
858 Depression, East Antarctica', *Journal of Geophysical Research: Oceans*, 109(11), p. C11003. doi:
859 10.1029/2004JC002441.
- 860 Massé, G. *et al.* (2011) 'Highly branched isoprenoids as proxies for variable sea ice conditions in the



- 861 Southern Ocean’, *Antarctic Science*, 23(5), pp. 487–498. doi: 10.1017/S0954102011000381.
- 862 Massom, R. A. *et al.* (2001) ‘Effects of regional fast-ice and iceberg distributions on the behaviour of
863 the Mertz Glacier polynya, East Antarctica’, *Annals of Glaciology*, 33, pp. 391–398. doi:
864 10.3189/172756401781818518.
- 865 Massom, R. A. *et al.* (2018) ‘Antarctic ice shelf disintegration triggered by sea ice loss and ocean swell’,
866 *Nature*. Springer US, (li). doi: 10.1038/s41586-018-0212-1.
- 867 Masson-Delmotte, V. *et al.* (2011) ‘A comparison of the present and last interglacial periods in six
868 Antarctic ice cores’, *Climate of the Past*, 7(2), pp. 397–423. doi: 10.5194/cp-7-397-2011.
- 869 Matsuda, H. (1978) ‘Early diagenesis of fatty acids in lacustrine sediments-III. Changes in fatty acid
870 composition in the sediments from a brackish water lake’, *Geochimica et Cosmochimica Acta*, 42, pp.
871 1027–1034.
- 872 Mayer, L. M. (1993) ‘Organic Matter at the Sediment-Water Interface’, in *Organic Geochemistry:
873 principles and applications*, pp. 171–184. doi: 10.1007/978-1-4615-2890-6_7.
- 874 McCartney, M. S. and Donohue, K. A. (2007) ‘A deep cyclonic gyre in the Australian-Antarctic Basin’,
875 *Progress in Oceanography*, 75(4), pp. 675–750. doi: 10.1016/j.pocean.2007.02.008.
- 876 McCave, I. N. and Hall, I. R. (2006) ‘Size sorting in marine muds: Processes, pitfalls, and prospects for
877 paleoflow-speed proxies’, *Geochemistry, Geophysics, Geosystems*, 7(10). doi: 10.1029/2006GC001284.
- 878 McCave, I. N., Manighetti, B. and Robinson, S. G. (1995) ‘Sortable silt and fine sediment
879 size/composition slicing: Parameters for palaeocurrent speed and palaeoceanography’,
880 *Paleoceanography*, 10(3), pp. 593–610. doi: 10.1029/94PA03039.
- 881 McKay, R. *et al.* (2016) ‘Antarctic marine ice-sheet retreat in the Ross Sea during the early Holocene’,
882 *Geology*, 44(1), pp. 7–10. doi: 10.1130/G37315.1.
- 883 Meyers, P. A. and Ishiwatari, R. (1993) ‘Lacustrine organic geochemistry-an overview of indicators of
884 organic matter sources and diagenesis in lake sediments’, *Organic Geochemistry*, 20(7), pp. 867–900.
885 doi: 10.1016/0146-6380(93)90100-P.
- 886 Mezgec, K. *et al.* (2017) ‘Holocene sea ice variability driven by wind and polynya efficiency in the Ross
887 Sea’, *Nature Communications*. Springer US, 8(1). doi: 10.1038/s41467-017-01455-x.
- 888 Nielsen, S. H. H. *et al.* (2007) ‘Origin and significance of ice-rafted detritus in the Atlantic sector of the
889 Southern Ocean’, *Geochemistry, Geophysics, Geosystems*, 8(12), p. n/a-n/a. doi:
890 10.1029/2007GC001618.
- 891 Pagani, M. *et al.* (2006) ‘Arctic hydrology during global warming at the Palaeocene/Eocene thermal
892 maximum’, *Nature*, 442(7103), pp. 671–675. doi: 10.1038/nature05043.
- 893 Paolo, F. S., Fricker, H. A. and Padman, L. (2015) ‘Volume loss from Antarctic ice shelves is
894 accelerating’, *Science*, 348(6232), pp. 327–331. doi: 10.1126/science.aaa0940.



- 895 Pollard, D. and Deconto, R. M. (2016) ‘Contribution of Antarctica to past and future sea-level rise’,
896 *Nature*, 531(7596), pp. 591–597. doi: 10.1038/nature17145.
- 897 Potter, J. R. and Paren, J. G. (1985) ‘Interaction between ice shelf and ocean in George VI Sound,
898 Antarctica’, in *Oceanology of the Antarctic Continental Shelf* (ed S. S. Jacobs), pp. 35–58. doi:
899 10.1029/AR043p0035.
- 900 Rhodes, R. H. *et al.* (2012) ‘Little Ice Age climate and oceanic conditions of the Ross Sea, Antarctica
901 from a coastal ice core record’, *Climate of the Past*, pp. 1223–1238. doi: 10.5194/cp-8-1223-2012.
- 902 Riaux-Gobin, C. *et al.* (2011) ‘Spring phytoplankton onset after the ice break-up and sea-ice signature
903 (Ad??lie Land, East Antarctica)’, *Polar Research*, 30(SUPPL.1). doi: 10.3402/polar.v30i0.5910.
- 904 Rignot, E. *et al.* (2013) ‘Ice Shelf Melting Around Antarctica’, *Science*, 1(June), pp. 1–15. doi:
905 10.1126/science.1235798.
- 906 Riis, V. and Babel, W. (1999) ‘Removal of sulfur interfering in the analysis of organochlorines by GC-
907 ECD’, *Analyst*, 124(12), pp. 1771–1773. doi: 10.1039/a907504f.
- 908 Robinson, N. J. *et al.* (2014) ‘Evolution of a supercooled Ice Shelf Water plume with an actively
909 growing subice platelet matrix’, *Journal of Geophysical Research : Oceans*, pp. 3425–3446. doi:
910 10.1002/2013JC009399.Received.
- 911 Sachse, D. *et al.* (2012) ‘Molecular Paleohydrology: Interpreting the Hydrogen-Isotopic Composition of
912 Lipid Biomarkers from Photosynthesizing Organisms’, *Annual Review of Earth and Planetary Sciences*,
913 40(1), pp. 221–249. doi: 10.1146/annurev-earth-042711-105535.
- 914 Schmidt, G. A., Bigg, G. R. and Rohling, E. J. (1999) *Global Seawater Oxygen-18 Database - v1.22*.
915 Available at: <https://data.giss.nasa.gov/o18data/>.
- 916 Schoemann, V. *et al.* (2005) ‘Phaeocystis blooms in the global ocean and their controlling mechanisms:
917 A review’, *Journal of Sea Research*, pp. 43–66. doi: 10.1016/j.seares.2004.01.008.
- 918 Schouten, S. *et al.* (2006) ‘The effect of temperature, salinity and growth rate on the stable hydrogen
919 isotopic composition of long chain alkenones produced by *Emiliania huxleyi* and *Gephyrocapsa*
920 *oceanica*’, *Biogeosciences*, 3(1), pp. 113–119. doi: 10.5194/bg-3-113-2006.
- 921 Sessions, A. L. *et al.* (1999) ‘Fractionation of hydrogen isotopes in lipid biosynthesis, Org’, *Organic*
922 *Geochemistry*, 30, pp. 1193–1200. doi: 10.1016/S0146-6380(99)00094-7.
- 923 Sessions, A. L. *et al.* (2004) ‘Isotopic exchange of carbon-bound hydrogen over geologic timescales’,
924 *Geochimica et Cosmochimica Acta*, 68(7), pp. 1545–1559. doi: 10.1016/j.gca.2003.06.004.
- 925 Shackleton, N. J. and Kennett, J. P. (1975) ‘Paleotemperature history of the Cenozoic and the initiation
926 of Antarctic glaciation; Oxygen and carbon isotope analyses in DSDP sites 277, 279 and 281’, *Initial*
927 *Reports of the Deep Sea Drilling Project*, 29, pp. 743–755. doi: 10.2973/dsdp.proc.37.1977.
- 928 Smethie, W. M. and Jacobs, S. S. (2005) ‘Circulation and melting under the Ross Ice Shelf: Estimates



- 929 from evolving CFC, salinity and temperature fields in the Ross Sea', *Deep-Sea Research Part I:*
930 *Oceanographic Research Papers*, 52(6), pp. 959–978. doi: 10.1016/j.dsr.2004.11.016.
- 931 Smith Jr., W. O. *et al.* (2012) 'the Ross Sea in a Sea of Change', *Oceanography*, 25(3, SI), pp. 90–103.
- 932 Solomina, O. N. *et al.* (2015) 'Holocene glacier fluctuations', *Quaternary Science Reviews*, pp. 9–34.
933 doi: 10.1016/j.quascirev.2014.11.018.
- 934 Spector, P. *et al.* (2017) 'Rapid early-Holocene deglaciation in the Ross Sea, Antarctica', *Geophysical*
935 *Research Letters*, 44(15), pp. 7817–7825. doi: 10.1002/2017GL074216.
- 936 Steig, E. J. *et al.* (1998) 'Changes in climate, ocean and ice sheet conditions in the Ross Embayment at 6
937 ka', *Annals of Glaciology*, 27, pp. 305–310. doi: 10.3198/1998AoG27-1-305-310.
- 938 Strickland, J. D. and Parsons, T. R. (1970) 'J. D. H. Strickland and T. R. Parsons: A Practical Handbook
939 of Seawater Analysis. Ottawa: Fisheries Research Board of Canada, Bulletin 167, 1968. 293 pp. \$ 7.50',
940 in *Internationale Revue der gesamten Hydrobiologie und Hydrographie*, pp. 167–167. doi:
941 10.1002/iroh.19700550118.
- 942 Tang, K. W. *et al.* (2008) 'Colony size of *Phaeocystis antarctica* (Prymnesiophyceae) as influenced by
943 zooplankton grazers', *Journal of Phycology*, 44(6), pp. 1372–1378. doi: 10.1111/j.1529-
944 8817.2008.00595.x.
- 945 Turner, J. *et al.* (2016) 'Antarctic sea ice increase consistent with intrinsic variability of the Amundsen
946 sea low', *Climate Dynamics*. Springer Berlin Heidelberg, 46(7–8), pp. 2391–2402. doi: 10.1007/s00382-
947 015-2708-9.
- 948 Wong, W. W. and Sackett, W. M. (1978) 'Fractionation of stable carbon isotopes by marine
949 phytoplankton', *Geochimica et Cosmochimica Acta*, 42(12), pp. 1809–1815. doi: 10.1016/0016-
950 7037(78)90236-3.
- 951 Zhang, J. and Hibler, W. D. (1997) 'On an efficient numerical method for modeling sea ice dynamics',
952 *Journal of Geophysical Research*, 102(C4), p. 8691. doi: 10.1029/96JC03744.
- 953 Zhang, Z., Sachs, J. P. and Marchetti, A. (2009) 'Hydrogen isotope fractionation in freshwater and
954 marine algae: II. Temperature and nitrogen limited growth rate effects', *Organic Geochemistry*, 40(3),
955 pp. 428–439. doi: 10.1016/j.orggeochem.2008.11.002.
- 956
957

958 **Acknowledgements:** Samples and data were provided by the International
959 Ocean Discovery Program (IODP). The Natural Environment Research Council funded K.E.A (CENTA
960 PhD; NE/L002493/1) and J.B. (Standard Grant Ne/I00646X/1). J.B. and O.S. were funded by Japanese
961 Society for the Promotion of Science (JSPS/FF2/60 No. L-11523). R.M. was funded by the Rutherford
962 Discovery Fellowship, the NZ Marsden Fund (RDF-13-VUW-003; 15-VUW-131) and Australia-New
963 Zealand IODP Consortium's Australian Research Council LIEF grant (LE0882854). A.C. was funded
964 by the NSF (PLR-1443347) and the U.S. Dept. of Energy (DE-SC0016105). A.C. performed model
965 integrations at the National Research Scientific Computing Center and at XSEDE, an NSF funded



966 computer center (grant ACI-1548562). C.R. was funded by a L'Oréal-UNESCO New Zealand For
967 Women in Science Fellowship, University of Otago Research Grant, and the IODP U.S. Science Support
968 Program. We thank S. Schouten, V. Willmott, F. Sangiorgi, J. Toney and J. Pike for discussions and V.
969 Willmott, H. Moossen, A. Hallander, R. Jamieson and C. Gallagher for technical support.

970
971 **Author contributions:** K.E.A., J.B and R.M. wrote the paper. J.B. and O.S. carried out the fatty acid
972 isotope analysis, A.A. and R.M. conducted the grain size analyses, J.E. and G.M. generated the HBI
973 data, F.J.J.E measured X-ray fluorescence scanning and electron microscopy, and C.R conducted the
974 opal measurements. R.D., R.M., X.C. and G.M. developed the age model. A.C ran the model
975 simulations. D.P.L and E.G analysed the Trace-21k experiment data. R.D. was lead proponent on the
976 U1357 drilling proposal. All authors contributed to the interpretations of data and finalization of the
977 manuscript.

978
979 **Competing interests:** The authors have no competing interests.

980
981 **Data availability:** There is no restriction on data availability. Upon manuscript acceptance, all
982 previously unpublished data will be added to the Supplementary Materials and made freely available at
983 the NOAA NCDC data-base: <https://www.ncdc.noaa.gov/data-access/paleoclimatology-data/datasets>.

984
985
986
987